Materials Chemistry and Physics 143 (2013) 116–123

Contents lists available at ScienceDirect

Materials Chemistry and Physics

journal homepage: www.elsevier.com/locate/matchemphys

The effect of noble gas bombarding on nitrogen diffusion in steel

E.A. Ochoa [a], R. Droppa [b], R.L.O. Basso [f], M. Morales [a], S. Cucatti [a], L.F. Zagonel [a], T. Czerwiec [c], M.C. dos Santos [d], C.A. Figueroa [e,*], F. Alvarez [a]

[a] Instituto de Física "Gleb Wataghin", Universidade Estadual de Campinas, 13083-970 Campinas, SP, Brazil
[b] Laboratório Nacional de Luz Síncrotron (LNLS), Campinas, SP, Brazil
[c] Institut Jean Lamour, Parc de Saurupt, 54042 Nancy Cedex, France
[d] Universidade de São Paulo, Instituto de Física, 05508-090, SP, Brazil
[e] Universidade de Caxias do Sul, CCET, 95070-560 Caxias do Sul, RS, Brazil
[f] Universidade Federal da Integração Latino-Americana, 85867-970 Foz do Iguaçu, PR, Brazil

HIGHLIGHTS

- Nitrogen diffusion enhancement by atomic attrition of Xe, Kr, and Ar.
- Atomic attrition modifies the microstructure well deeper than the ion implantation range.
- The stress is compressive in the implanted zone and tensile underneath over few 100 s nm.

ARTICLE INFO

Article history:
Received 9 February 2013
Received in revised form
22 July 2013
Accepted 16 August 2013

Keywords:
Nitrides
Diffusion
XPS
Mechanical properties
Surfaces

ABSTRACT

The low energy (~50–350 eV) noble gases ion bombardment of the steel surface shows that the pre-treatments increase nitrogen diffusion by modifying the outermost structure of the material. The surface microstructure and morphology of the studied samples were characterized by Scanning Electron Microscopy (SEM) and Atomic Force Microscopy (AFM). The crystalline and chemical structures in the outermost layers of the surface were analyzed by grazing angle X-ray diffraction (GAXRD) and photoemission electron spectroscopy (XPS). Temperature effusion studies of the implanted ions are used to elucidate the noble gases site localization in the network. The *local* compressive stress induced by the nearby iron atoms on the core level electron wave functions of the trapped noble gases are studied by photoemission electron spectroscopy (XPS) and interpreted considering a simple mechanical model. Nano-hardness measurements show the dependence of the material elastic constant on the energy of the implanted noble gases. Although the ion implantation range is about few nanometers, the atomic attrition effect is larger enough to modify the material structure in the range of micrometers. Two material stress zones were detected where the outermost layers shows compressive stress and the underneath layers shows tensile stress. The implanted noble gases can be easily removed by heating. A diffusion model for polycrystalline-phase systems is used in order to discuss the influence of the atomic attrition on the N diffusion coefficient. The concomitant effect of grain refining, stress, and surface texture on the enhancing nitrogen diffusion effect is discussed.

1. Introduction

Plasma nitriding is based on low energy nitrogen ion implantation and temperature activated diffusion [1–3]. The technique is broadly used for increasing hardness, corrosion resistance and improving tribological properties of a number of metallic alloys for technological applications. The process time span from few hours up to several days and diminishing the relative long processing times is a challenge if we want to increase the applications of the technique. The efficiency of the process and the final material properties are strongly dependent on defects at the surface created by ion impact. Recently, it has been shown that adequate combination of low energy nitrogen ions and substrate temperature modified the kinetic of the surface phenomena, decreasing the process time [4]. Also, mechanical attrition ("shot-peening") generating stress, plastic deformation and defects modify the surface chemical kinetic of the reactions, shortening nitriding process [5,6]. Similar effects were reported bombarding the samples with

* Corresponding author. Tel.: +55 54 32182764, +55 54 91796022 (mobile).
E-mail addresses: cafiguer@ucs.br, carlos.cafiguer@gmail.com (C.A. Figueroa).

0254-0584/$ – see front matter © 2013 Elsevier B.V. All rights reserved.
http://dx.doi.org/10.1016/j.matchemphys.2013.08.027

relative low energy xenon ions ("atomic attrition"). Indeed, increased hardness up to ~40% was reported by choosing a suitable set of the bombardment ion parameters [7]. The increasing number of boundary paths in the refined grain structure of the surface is probably the main cause of shortening the time in the nitriding process [8]. Results reported by Abrasonis et al. suggest that the effect of bombarding the material after nitriding has profound consequences on N diffusion in metals [9]. In a recent fine experiment Zhang et al. have shown that low energy (500 eV) Ar^+ ion irradiation significantly increased the Ni diffusion in Cu at distances much deeper than the affected radiated surface [10]. Finally, Martinavicius et al. showed the influence of ion irradiation on nitrogen diffusion in stainless steel [11]. These authors invoke highly anharmonic localized excitations (such as a Discrete Breath) which can propagate distances well beyond the ion penetration depth to explain generation of deeper defects and thus probably increasing the effective diffusion coefficient.

In this paper, by employing various techniques we have extended our previous work with Xe to a comprehensive investigation on the surface properties of steel bombarded with other low energy ions (Xe, Kr, and Ar). Specifically, the effect of the atomic attrition on the *in situ* posterior nitriding process is discussed. The microstructure and morphology of modified surface were correlated to the crystalline and chemical structure of the outermost layers. Finally, applying a standard model of poly-phase diffusion mechanism, the N equivalent diffusion coefficient due to the atomic attrition effect is estimated and compared with those values obtained in not pre-bombarded samples.

2. Experimental

The experiments were performed in mirror polished, rectangular samples, 20 × 10 mm and 1 mm thick, prepared from the same commercial AISI 4140 steel lot (C: 0.4, Si: 0.25, P: <0.04, S: <0.04, Mn: 0,85, Mo: 0.20, Cr: 1, Fe: balance). The noble gases bombarding and nitriding experiments were carried out in a high-vacuum system ($<10^{-7}$ mbar) attached to an ultra high vacuum chamber ($<2 \times 10^{-9}$ mbar) for XPS analysis. The deposition chamber contains a 3 cm diameter DC Kaufman ion source. Details of the apparatus are described elsewhere [12].

All the studied samples were introduced in the IBAD chamber after 10 min cleaning in acetone ultrasonic bath. Before starting the implantation of each NG, the samples were also cleaned by five (5) minutes, 1 keV ions (Ar^+, Kr^+, or Xe^+) sputtering, at room temperature. We note, also, that the low background oxygen partial pressure in the IBAD ($<10^{-8}$ mb) chamber makes unnecessary de use of hydrogen as reducing agent [13].

Before nitriding, the surface of the substrate is textured as a consequence of NG bombardment (atomic attrition) during 30 min at room temperature with fixed energies selected between 50 and 350 eV and ion current density of 1 mA cm^{-2}. Immediately after this pre-treatment, the substrate temperature is raised to the working nitriding temperature (380 ± 5) °C. This process takes approximately 15 min. Subsequently, the sample is irradiated with a pure nitrogen ion beam of 1 mA cm^{-2} and constant energy (200) eV during 30 min. The substrate temperature is measured at the surface of the sample by an optical pyrometer (Raiomatic 20, IRtec, Eurotron) focused on the sample surface by a He–Ne laser. A thermocouple located on the substrate holder gives a signal feeding proportional–integrator–differential (SPH Temperature Controller, England) feedback systems controlling the temperature of the substrate holder.

The morphology of the samples before and after the atomic bombardment was analyzed by field emission gun-scanning electron microscopy (FEG-SEM), atomic force microscopy (AFM), and optical microscopy. In order to study the activation energy barrier during isochronal temperature effusion of the NG atoms trapped in the steel matrix, a set of samples were irradiated with the Xe^+, Kr^+, and Ar^+ at room temperature and afterward annealed for a controlled degasification. All the treated samples were routinely characterized by XPS [14]. The hardness profiles and nano-indentation module were obtained by nano-indentation using a Berkovich diamond tip (NanoTest-300). The load–displacement curves were analyzed using the Oliver and Pharr method [15]. In a previous work, the nitrogen profiles of nitrided samples (without pre-treatment) and nitrided after Xe^+ bombardment were obtained by Secondary Neutral Mass Spectroscopy (SNMS) [7]. These results were further analyzed in order to obtain the nitrogen diffusion coefficient in the material. The cross section of the samples treated with Kr^+ and Ar^+ was studied by FEG-SEM after a 10 s attack with Nital solution (5% nitric acid in ethanol). For comparison purposes, the cross section of the sample bombarded with Xe^+ and studied by FEG-SEM was reproduced and adapted from the work by Ochoa et al. [7]. For the phase identification and stress studies, both normal and grazing X-ray diffraction experiments were performed using synchrotron radiation. The evolution of the nitrides phases due to the noble gases pre-bombardment treatment was gathered at a $\theta = 2^\circ$ grazing angle in a Bragg–Brentano X-ray diffraction configuration and a monochromatized Cu-Kα radiation line (Shimadzu, LAB X-XRD-6000). For residual stress analysis the XRD experiments were performed using grazing synchrotron radiation in the Seemann–Bohlin (SB) geometry [16]. The method used for the study was the "g-sin$^2\psi$ method", where ψ is the angle between the diffracting planes and the sample surface [16–18]. In order to study the N diffusion in the bombarded samples, we apply the classical Fick's laws to nitrogen diffusion process in steel, considering it as polycrystalline multiphase system [19].

3. Results and discussion

3.1. Morphology of samples before and after ion bombardment by SEM and AFM imaging

As remarked above, atomic attrition can induce grain refining from micrometric particles up to fractions of a micron on the bombarded surface sample. As an example of in cross-section microstructure modification, Fig. 1a, b1 and c1 shows the FEG-SEM micrographs of Xe^+, Kr^+, and Ar^+ ion bombarded samples with energies of 125 eV, 150 eV, and 100 eV, respectively. As we shall show below (Section 3.2), these energies produce the maximum local stress around the implanted NG. In order to analyze further the influence of atomic attrition in the material microstructure, the pristine sample in cross-section was studied by FEG-SEM where neither atomic attrition nor nitriding treatments were performed (please, see Fig. 1b2 and c2).

On the one hand, the pristine sample shows a characteristic microstructure of ferrite and pearlite for a low-alloy steel as AISI 4140. In both Fig. 1b2 and c2, one can see that ferrite and pearlite grains are the same, in terms of microstructure and morphology, either near surface or deeper in depth. On the other hand, the FEG-SEM images in Fig. 1a, b1 and c1 shows a pattern of layered structures formed mainly by micrometric and sub-micrometric grains where the original microstructure of ferrite and pearlite was totally degraded. Indeed, it is clearly seen in Fig. 1b1 and c1 that the lamellas of the original pearlite structure are smaller and shorter with a random distribution. Fig. 1a–c shows that the atomic attrition modifies the microstructure of the original material in the range of micrometers. This relatively high depth outcome cannot be explained by cascade effect of the so call "replacement collision sequence". This effect has been evoked as causing stress in thin films growth [20]. Indeed, molecular dynamics studies have shown

that such sequences occur along no more than a hundred atomic distances, which is far below the order of a micrometer experimentally observed effects [21]. As we shall see below, the hardness of the material is also in depth modified by the bombardment (Sections 3.3 and 3.6).

Fig. 1d1 shows the AFM images of a sample bombarded with Ar^+ ions (150 eV) energy. Fig. 1d2 is a detail of the same sample. One can note that several different direction periodic patterns are displayed on the picture. The direction of the pattern periodicity depends on the grain crystalline orientation, i.e., the ionic bombarding generates a periodic arrangement following the crystalline orientation of the grains. This behavior is explained by the Ehrlich–Schwoebel instability model [22]. Roughly speaking, the combined effect of sputtering and surface diffusion barriers in metals induces the formation of periodic structures following the crystalline grain orientation as those observed in Fig. 1.

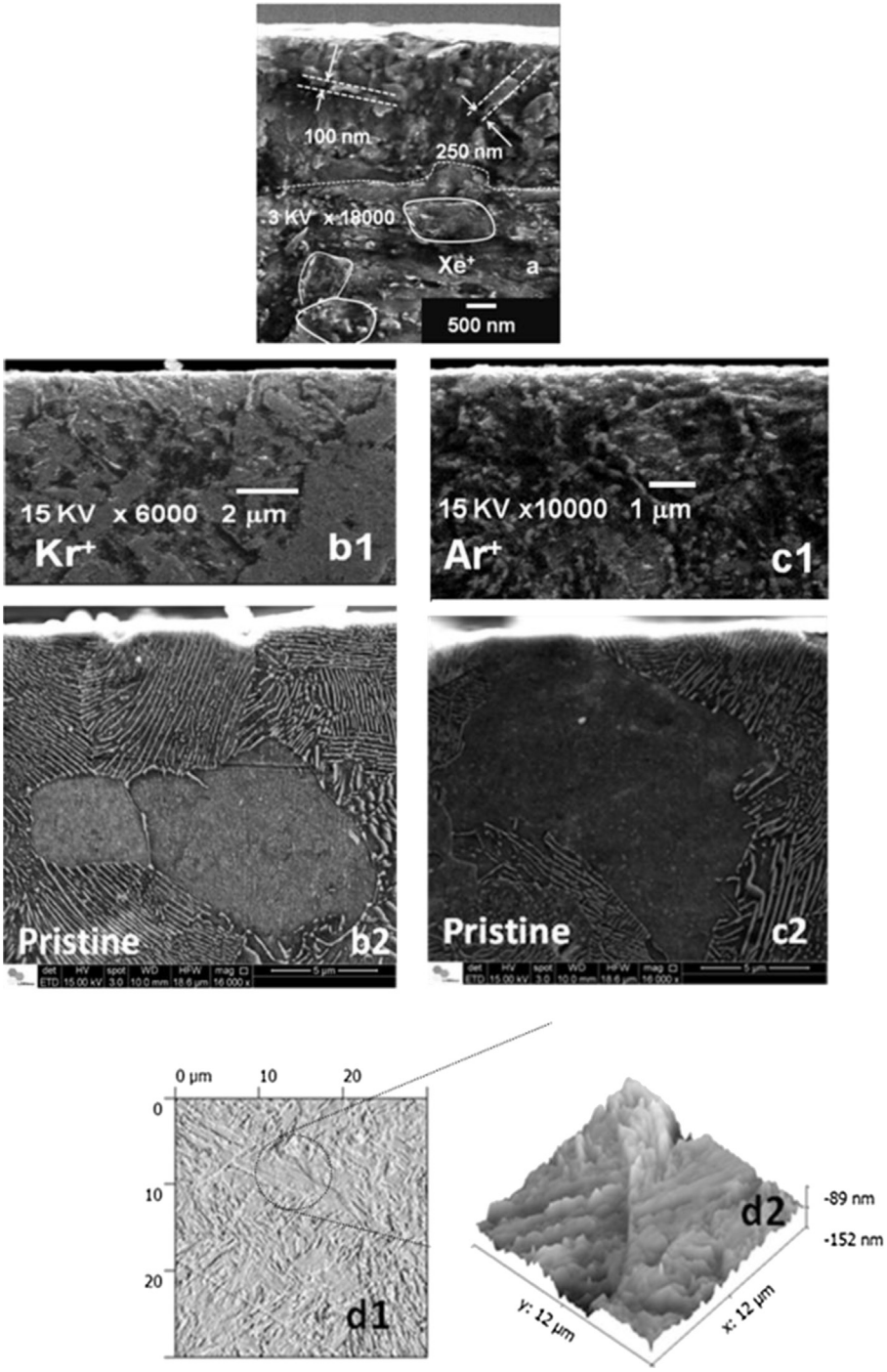

Fig. 1. FEG-SEM images in cross-section of Xe^+ (a), Kr^+ (b1), and Ar^+ (c1) bombarded sample with 125 eV, 150 eV, and 100 eV, respectively. The enlarged micrograph (a) clearly shows modified structure induced by Xe^+ bombardment (adapted from Ref. [7]). The chosen bombarded energies are those producing maximum local stress (Section 3.5). Pictures (b2) and (c2) are two different regions of the same pristine sample (without any treatment) where a characteristic microstructure of ferrite and pearlite is apparent. In (a), a couple of the refined grains are rounded by a dashed loop. A fracture produced by the bombardment is indicated by a wavy dashed line. Larger grains less affected by the bombardment are rounded with a continuous line. (d1): AFM image of a sample bombarded with Ar^+ ions 150 eV energy; (d2): detail from the same sample.

Table 1
r_{NG}/r_T and r_{NG}/r_O: ratios between the NG (r_{NG}, covalent radius) and interstices sites radii r_T and r_O. $r_T = 0.29$ and $r_O = 0.15$ are the radius of the α (bcc) tetrahedral (T) and octahedral (O) interstices sites in iron atomic radius units, respectively (the covalent radii r_{NG} of the NG atoms is adopted for comparison purposes) [27].

NG	r_{NG}/r_T	r_{NG}/r_O
Xe	4.48	8.66
Kr	3.79	7.33
Ar	3.34	6.46

3.2. Chemical environment study by XPS

The interaction among the implanted NG atoms and the nearby atoms of the network is manifested as an energy shift $\Delta\varepsilon$ ("chemical shift") of the binding energies associated with the core-level electrons of implanted atoms [23]. Therefore, the XPS spectra reflect the *local* influence of the nearby host atoms on the trapped NG and the obtained information comes from ~50 Å, i.e., the escape mean free path of the ejected photoelectrons [23]. As we shall discuss it in Section 3.5, after a few collisions, the projectile probably occupies an interstitial site in the α (bcc) host crystal, causing a *local* stress related to the atom size misfitting [24]. In Fe atomic radius units, the size of the α (bcc) tetrahedral (r_T) and octahedral (r_O) interstitial sites are 0.29 and 0.15, respectively (Table 1) [25]. They are compared in Table 1 with the NG covalent radii. Therefore, due to the stress caused by the misfitting atoms in the host crystal, the binding energy (BE) of the Xe $3d_{5/2}$ electrons changes [26,27]. Moreover, the observed chemical shift decreasing the binding electron energy indicates a compression of the electronic cloud density of the implanted NG, i.e., higher electronic density increases the electron repulsion making it easier to eject an electron from the element core level.

Fig. 2a shows the spectra corresponding to the electrons Xe $3d_{5/2}$ and Xe $3d_{3/2}$ for different implantation energies. Similar curves are obtained for Kr^+ and Ar^+ bombarded samples (not shown). The expected position energies for the corresponding levels in the gas phase are indicated in the figure [28]. Fig. 2b shows the corrected chemical shift $\Delta E = \Delta\varepsilon - RE$ vs. implantation energy for the Ar 2s, Kr $3p_{3/2}$ and Xe $3d_{5/2}$ electron levels of all the studied samples (note that, in this plot, the work function is not included). A local maximum in this curve is observed in this figure compatible with stronger interaction of the NG with the host crystal, phenomenon associated with the material stress induced by trapped NG. In fact, the fitted curves in Fig. 2b were obtained by applying a model which will be discussed latter at the end of Section 3.5, which supports the dependence of material stress on trapped NG. On the other hand, for greater bombardment energies, the interaction leads to material relaxation. As observed in the plot, all these effects are stronger in the case of Xe due its larger atomic radius. Indeed, Fig. 2 shows that the chemical shift depends on bombardment energy and the type of projectile.

3.3. Mechanical properties I. Nano-indentation studies

Fig. 3 shows the hardness and nanoindentation module as a function of the implantation energy of Xe ions obtained by nano-indentation measurements at fixed depth of 100 nm, i.e., much deeper that the region probe by XPS (~5 nm). Moreover, according to simulations using TRIM, the projectile implantation zone (IZ) in the Fe matrix is around ~5–10 Å [29,7]. Consequently, the replacement collision sequence effects during ion implantation could explain both hardness and nanoindentation module behaviors far away from IZ [7]. As we shall see in Section 3.6, the atomic attrition modifies the material up to ~1.5 μm in depth. This result suggests two things. First, the ion implantation process penetrating up to 10 Å in depth induces deeper changes in the material (at least ~100 nm). Second, the hardness of the material has also a maximum value at the same bombarding energy giving the largest chemical shift (Fig. 2). We also note that the nanoindentation module obtained from the nano-indentation experiments are higher than the ~200 GPa value normally reported for the studied AISI 4140 steel [30]. A similar behavior to the one described for the samples treated with Xe^+ is observed in samples bombarded with Ar^+ and Kr^+ albeit less intense (not shown). We shall come back to the hardness profile of the studied samples in Section 3.6.

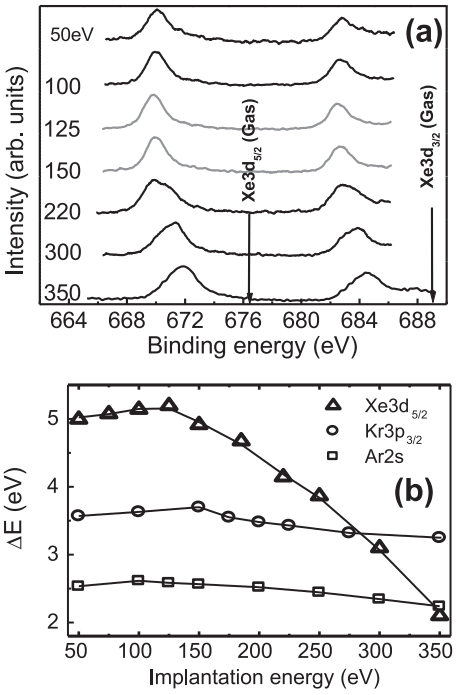

Fig. 2. (a) XPS spectra for the core levels Xe $3d_{5/2}$ and Xe $3d_{3/2}$ of xenon for different implantation energies. The shifts of peaks are taken with respect to the corresponding gas phase energies. (b) Experimental binding energy shifts $\Delta E = \Delta\varepsilon - RE$ of the selected electron core levels (relative to the gas phase) of NG vs. implantation energy. The relaxation energy of the system was considered as explained in the text. Note that in this plot the work function is not included. The solid line corresponds to the fitting of a theoretical stress expression resulting by the *knock on* implanted atoms and thermal spikes relaxation (see Section 3.5).

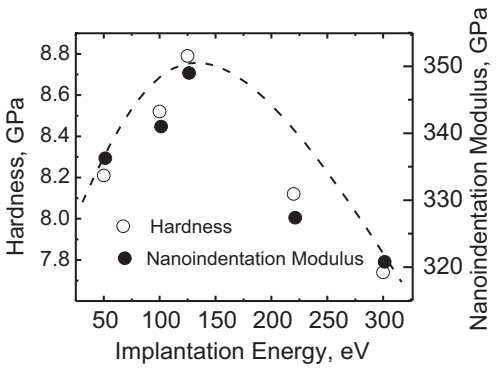

Fig. 3. Nano-hardness (at 100 nm depth) and nanoindentation modulus vs. implantation energy of Xe ions. The dashed line is a guide for the eyes.

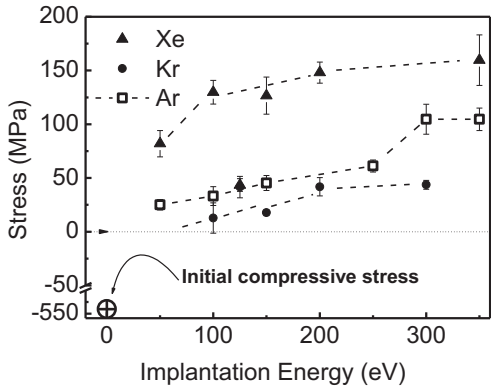

Fig. 4. Residual stress on the iron lattice for Ar^+, Kr^+, and Xe^+ treatments obtained from synchrotron X-ray diffraction measurements. The compressive stress (circle with a cross) of the original material is also shown.

3.4. Mechanical properties II. Samples residual stress obtained from synchrotron X-ray grazing diffraction

As described in Section 2, the residual stress present in different oriented grain populations can be obtained by X-ray diffraction (XRD) using the Seemann–Bohlin (SB) geometry. The use of X-rays to study the sample stress complements the information obtained from the electron core level of the implanted NG. As discussed in Section 3.2, the XPS is a local probe since the chemical shift is sensitive to the local influence of the nearby Fe atoms on the electronic cloud of the implanted NG. Moreover, as noted in Section 3.2, the XPS technique is probing electrons being ejected up to ~50 Å depths [23]. On the other hand, the X-ray measurement gives a bulk insight into the state of the tensions of the sample. Moreover, since the grazing angle used in the experimental set up gives information from ~1 μm in depth, the measured stress represents the state of tensions of the material well below the top most layer (~5–10 Å) containing the trapped NG.

Fig. 4 shows the residual stress values obtained for the samples bombarded with Xe^+, Kr^+, and Ar^+ at different implantation energies following the procedure outlined in Section 2. For comparison purposes, the residual stress of a pristine sample is also shown in the graph (filled dot). From this plot, the following observation are drawn regarding the state of the tensions of the material beneath the surface: a) the high negative value indicates that the raw samples originally have a compressive residual stress, probably due to the cutting and polishing process [31]; b) the residual stress below the thin implanted surface (i.e., >>5 Å) of the samples changes from compressive to tensile due to the ion bombardment; c) for the lighter NG projectiles studied, the residual stress is barely resolved from the experimental error; e) for Xe^+, Ar^+ and Kr^+ there is a *trend* to increase tensile stress on ion energy bombardment. The stress obtained for the sample bombarded with 125 eV is completely shifted from the general trends. Unfortunately the limited time of the synchrotron radiation prevented us to repeat these measurements. Nevertheless, although more work is necessary, we suggest that the general trend is correct since the majority of the calculated stresses shown in Fig. 4 are consistent. From the information gathered, the state of the tension of the bombarded sample is schematically represented in Fig. 5a. The thin top most layers represent the ~5 Å containing the trapped NG submitted to a compressive stress (*knock-on* effect [32,33]) whereas below this implanted region, the thicker layer is submitted to a tensile stress. The compressive stress is confirmed by the negative chemical shift of the electrons core level of the trapped NG atoms (Section 3.2, Fig. 2b). Fig. 5b helps to understand this comment. Assuming it is free of constrainers, the top layer is assumed to be larger by $\Delta L = L - L_0$ than the original sample size due to the presence of implanted NG (Fig. 5b, top). In order to fit the actual sample size L_0, a parallel force to the surface is necessary, i.e., the bulk substrate is applying a compressive stress to the implanted layer (Fig. 5b, middle). Therefore, in order to satisfy the equilibrium condition, the bulk material suffers a tensile stress (Fig. 5b, bottom).

3.5. Effusion experiments

In the attempt to identify the localization site of the implanted NG and its relation with electron core level energy shift measured by XPS, we have performed isochronal annealing experiments. For each type of implanted atom (Xe, Kr, and Ar), six samples were studied, i.e., three sets of six samples were prepared. One at a time, a sample of each set is then bombarded during 30 min using the energy corresponding to the maximum chemical shift displayed in Fig. 2b. As commented above, the XPS technique probes the surface up to ~50 Å of the material, i.e., the NG atoms are trapped within the studied region. After bombarding, the sample is immediately transferred to the UHV chamber for XPS measurements. Afterward, the sample is returned to the bombarding chamber and annealed during 5 min in the implantation chamber at 100 °C and again transferred to the UHV for a new XPS measurement. This procedure is then repeated for each freshly bombarded sample of each set in increasing steps of 50 °C (i.e., 100, 150, 200 °C etc.) and maintaining the annealing time constant (5 min). Our results have shown that after the 350 °C annealing step practically all the implanted gases abandoned the material preventing further measurements, i.e., the remaining if any, is below the detection limit of our apparatus (<0.3%). In order to simplify the analysis of this process, a simple model considering the diffusion of holes into the sample instead of particles leaving the sample will be considered. In other words, introducing a hole is equivalent to extract a NG atom from the sample. Assuming a semi-infinite plate, the amount of holes diffused in the material at time t is characterized by the mass $M(T) = 2c^*[D(T)\ t]^{1/2}$ [34]. Here c^* is the concentration of hole (reservoir) assumed constant at the free surface and $D(T)$ is the hole diffusion coefficient. Then, the effusion rate can be studied by isochronal annealing of the sample at a temperature T and by measurements of the remaining band area. Therefore, the total amount of NG atoms is a function of the area $A = A_0 - 2pc^*[D(T)\ t]^{1/2}$, where p is a proportional constant and A_0 is the starting band area, i.e., before the annealing. Now, considering that $D(T) = D_0 e^{-E_A/kT}$, where E_A and k are the activation energy and the Boltzmann constant, respectively, the dependence of NG in the material on T and t is:

$$\mathrm{NG}(t,T) \sim A = A_0 - 2pc^*(D_0 t)^{1/2} e^{-E_A/2kT} \quad (1)$$

The stronger exponential dependence on temperature allows us to estimate the activation energy E_A of the effusion process by plotting ln A *vs.* $1/T$. In this way, one can assume that the area under the XPS bands associated with the NG electrons core level, are proportional to the remaining atoms concentration in the material after the effusion procedure. Fig. 6a shows the plot for the corresponding areas vs. the inverse of temperature, T^{-1}. Fig. 6b represents the activation energy of the studied implanted gases vs. the atomic mass obtained from the Arrhenius plots. For comparison purposes, the activation energy of implanted He^+ obtained from the literature is included [35]. The nice straight line clearly suggests that the effusion process in the studied region is controlled by the size of the implanted noble atom.

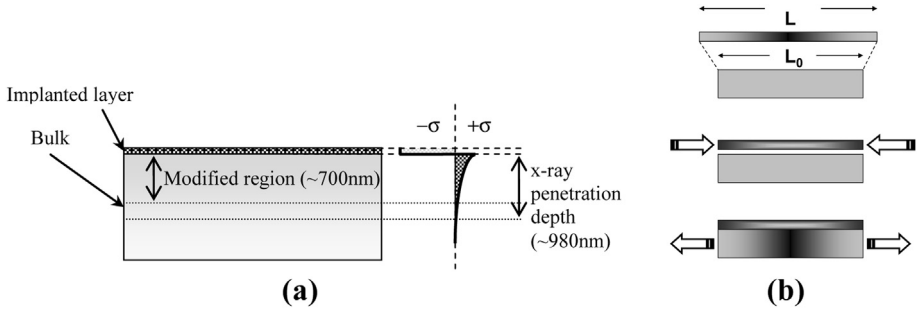

Fig. 5. (a) Schematic representation of the state of the tensions along the direction perpendicular to the sample. The thin implanted layer has a compressive stress ($-\sigma$) while the bulk layer below it is submitted to tensile stress ($+\sigma$). (b) The schematic shows the origin of the stress. Top: L and L_0, expanded "free" implanted and bulk layers, respectively. Middle: compressive stress of the implanted layer to fit the bulk material. Bottom: in equilibrium, the implanted layer is compressed and the bulk layer stretched.

The relatively low values of the activation energy suggest an interstitial site for most of the trapped NG atoms rather than occupying a Fe host atom, either in octahedral or tetrahedral sites. Considering that the bonds involved in the tetrahedral sites are stiffer than the bonds in octahedral ones, the latter cavities are a stronger candidate to host the implanted NG.

The activation energy obtained from the effusion experiments can be related to the core level electron binding energy shift observed by XPS. Furthermore, the residual stress in the most top layers is a result of competition between the *knock on* phenomenon generating a stressed meta-stable site and local relaxation by thermal spike [32,33]. Indeed, due to thermal spikes, the implanted NG atom can suffer thermo-activated hops with activation energy E_0 given by $(E/E_0)^{5/3}$, i.e., the trapped NG has some probability to escape into the vacuum chamber, minimizing the total network energy [33]. Davis has shown that the fraction of trapped atoms (n/N) strains the host material network, generating a stress σ is given by $\sigma \sim [Y/(1-\nu)]E^{1/2}/[\alpha + \beta(E/E_0)^{5/3}$ [33]. Here Y is the nano-indentation modulus, E the ion energy, ν the Poisson ratio and α, β are constants. Fig. 2b reproduced the binding energy shift vs. Ion Energy (open triangles) for the energy shifts associate to samples bombarded with Xe^+. Assuming the stress being proportional to the observed chemical shift, the solid line corresponds to the fitting the above equation for σ, assuming $E_0 \sim 126$ meV, i.e., the activation energy estimated from the effusion experiment (Fig. 6). The plot shows a quite good fitting to the experimental data. Finally, it is important to remark that this result apply to the top of the sample, i.e., ~5 Å depth, region where the Xe atoms are trapped during implantation.

3.6. Bombarding effect on the nitriding process

In this section we shall study the consequences of the heavy atoms bombardment on the nitriding process. As described in Section 2, the evolution of the nitride phases due to the noble gases pre-bombardment treatment was gathered at a $\theta = 2^\circ$ grazing angle by using a standard diffractometer in a Bragg–Brentano geometry. In this case, the penetration depth is estimated to be ~0.15–0.20 μm i.e., the probed region is in the modified surface by ion bombardment. Although the comparison of X-rays diffractogram intensities must be taken carefully, we shall discuss some results that, in conjunction with other experiments, reinforce the conclusion that the atomic attrition enhances nitrogen diffusion. Fig. 7 shows grazing angle diffractograms of the nitrided samples with and without previous NG atom bombardment. In order to be able to compare the diffractograms, care was taken in the preparation of the samples and in the reproducibility of the diffraction measurements. The curves are normalized to the intensity of the α reflection peak. From this plot one can estimate that the pre-treatment enhances the presence of the γ'-Fe_4N and ε-$Fe_{2-3}N$ phases at the surface of the material as a function of the noble gas atomic mass. Indeed, the roughness of the surface is probably contributing to augment the nitrogen retention on the surface during the nitriding process, as well as the refining grains create new diffusion channels and the

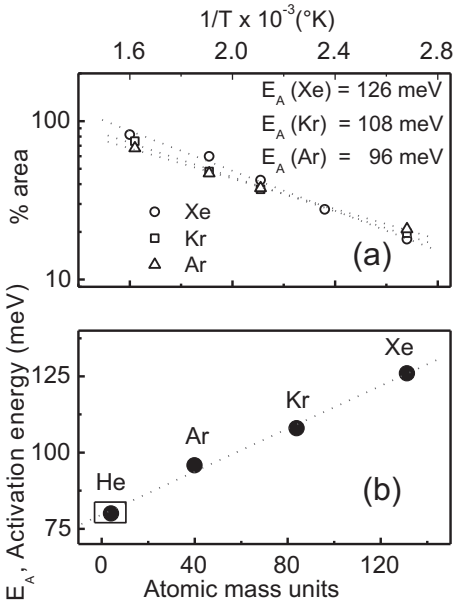

Fig. 6. (a) Arrhenius plot for the Ar, Kr and Xe effusion experiments. The experimental error is of the order of the symbols. (b) E_A vs. atomic masses.

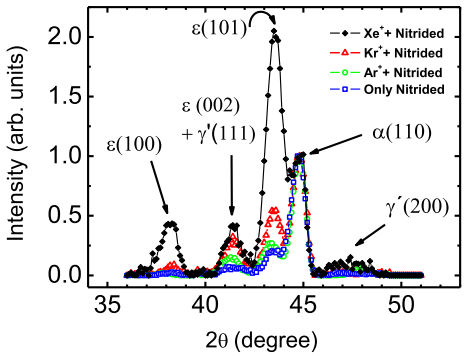

Fig. 7. Grazing angle diffractograms of samples 30 min simultaneously nitrided with and without pre-treatment bombardment.

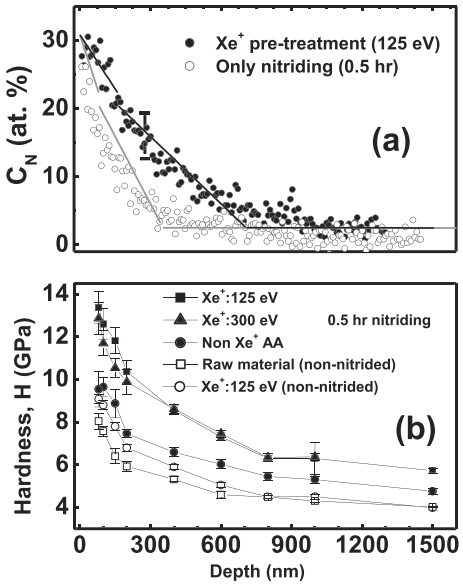

Fig. 8. (a) Nitrogen profile of nitrided samples with and without previous Xe^+ bombardment (125 eV) reproduced from Ochoa et al. [7]. In both cases the nitriding time was 0.5 h; (b) Hardness vs. depth for nitrided samples (solid symbols) and non-nitrided samples (open symbols).

Table 2
Diffusion coefficient for nitrogen in the gamma line phase obtained for the nitrated (380 °C) samples with and without pre-treatment (AA, Xe^+: 125 eV, 0.5 h).

	I = without pre-treatment	II = with pre-treatment (AA)	Ratio II/I
$D_{\gamma'}$ ($\mu m^2\ s^{-1}$)	$(0.8 \pm 0.2) \times 10^{-5}$	$(1.7 \pm 0.1) \times 10^{-5}$	2.1 ± 0.6

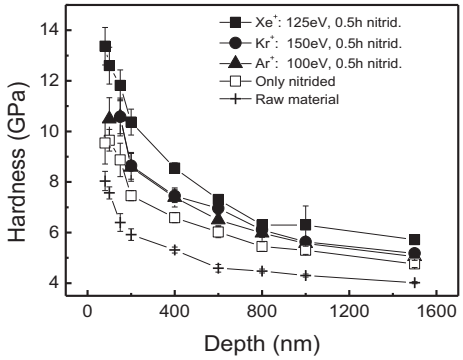

Fig. 9. Hardness vs. depth for different NG pre-treated samples. The hardness of the raw material and that of nitride samples without pre-bombardment are also shown for comparison purposes.

surface texturization increases the nitrogen concentration at the material surface, altogether improving the nitrogen diffusion.

It is interesting to quantify the influence of the atomic attrition on the process and on the diffusion coefficient of N in the bombarded material. In Fig. 8a and b, we reproduce results previously reported on nitrogen concentration and hardness profiles of the nitride samples after bombarding, respectively [7]. The nitrogen profiles were obtained by Secondary Neutral Mass Spectroscopy (SNMS) for two nitrided samples with and without atomic attrition pre-treatment of Xe^+ ions (Fig. 8a). For completeness, the hardness profiles obtained by nano-hardness measurements from the cited study are also reproduced (please, see Fig. 8b). As commented in the introduction, to estimate the effective diffusion coefficient, we apply the classical Fick's laws to nitrogen diffusion process in steel, considering it as polycrystalline multiphase system [19]. This model permits obtain the effective diffusion coefficient as an adjustable parameter by fitting the expressions of the nitrogen concentration given by $C(x,t) = k_1 + k_2\ \mathrm{erf}(x/2\sqrt{Dt})$ to the experimental profiles. Here x is the distance measured from the sample free surface, t the nitriding process time, k_1, k_2 constants and D the diffusion coefficient D, all of them adjustable parameters. The experimental concentration data dispersion makes the fitting in the region where the ε- and α-phase are expected dubious. In fact, the large standard deviation makes uncertain the determination of the diffusion coefficient. Therefore, we report only the results concerning the diffusion coefficient obtained in the nitrogen concentration range where is expected the γ-phase and the experimental profiles are clearly resolved (Table 2).

The plot shows in Fig. 3 that the attrition *per se* induces a moderate hardness increasing due, might be, to the stress generated by the ion bombardment (AA). As expected, these results are reflected in the hardness of the studied samples (Fig. 8b). Fig. 9 shows the hardness profile for nitrided samples after pre-bombardment at the ion energy which maximizes the chemical shift of the implanted noble gases. We note that, under some assumptions, the hardness profiles can be used to estimate the nitrogen concentration in the material [19,36]. In a previous paper was shown that for the material studied in this paper the hardness H is proportional to the in-depth nitrogen concentration, i.e., $H(\mathrm{GPa}) \cong m[\mathrm{N}] + 4(\mathrm{GPa})$, where $m = 0.54$ and [N] are the slope and nitrogen concentration measured in GPa/at% and at%, respectively [7]. Therefore, the curves in Fig. 9 are approximately mapping the nitrogen profiles of the studied samples. Thus, these curves show that nitrogen diffusion is enhanced when heavier noble gases are used in atomic attrition pre-treatments.

As pointed out above, TRIM simulations show that the ion penetration is ~5–10 Å [7]. However, by observing the curve in Fig. 8b, one can see that hardness induces by the bombardment propagates as far as ~700 nm. We note, also, that the hardness slightly increases on increasing atomic mass of the projectile. On the one hand, the hardness profiles in all the pre-bombarded and nitride samples expand deeper than in those samples without previous atomic attrition. Indeed, the bombardment "long range" effects with high ion energies (>keV) are known and several experimental papers are published on the subject [37,38]. On the other hand, studies involving low energy ions bombardment like the results reported in this paper are scarce. As commented above, highly anharmonic localized excitations (such as a Discrete Breath) which propagate distances well beyond the ion penetration depth were invoked to explain creation of deeper defects enhancing nitrogen diffusion [9]. However, more work is necessary before having a clear understanding of the experimental findings.

In the attempt to explain the nitriding enhancement process in pre-treated samples we suggest that it is due to not only by one independent effect but also by a conjunction of the following mechanisms: first, grain refining effect of the bombardment, i.e., increasing inter-grain diffusion path (see Fig. 1a) [5,8,39]; second, the texturized surface of the material probably increases the surface nitrogen retention (Fig. 1d). Finally, the tensile stress discussed in Section 3.4 can contribute to enhancing N diffusion [40]. Indeed, tensile stress allows stretching further the crystalline unit cells of modified layer, increasing the mean free path for nitrogen interstitial diffusion.

4. Conclusions

Low energy NG ion bombardment of steel substrate at room temperature modifies the structure of the material surface. The effect

of the bombardment goes orders of magnitude beyond the thin implanted zone. *Ex situ* scanning electron, atomic force microscopies (FEG-SEM, AFM) and X-ray analysis show that the NG bombardment refines the underneath grains, texturizes the surface and strains the material. The strain is a consequence of the energy transferred by the projectile and the occupancy of small spaces by the massive NG ions (misfitting). The combined effect of sputtering and surface atoms diffusion induces the formation of characteristics patterns (texture) contributing to increase nitrogen retention at the material surface during the nitriding process. The local stress generated by the mismatching trapped NG atoms is evidenced by the core level cloud compression and decreasing binding energy associated with the NG electrons core level levels. The strain increases as a function of the atomic mass of the NG. By diffraction grazing angle studies, a tensile stress in depths is observed to be orders of magnitude larger than the physically modified underneath thin noble gases implanted layer. This tensile stress can contribute to increase the diffusion of N by opening the crystal network. The relatively low activation energies of the trapped gases effusion on annealing experiments suggest the interstitial localization of the NG atoms in the lattice. Due to these low activation energies no traces of noble gases are found after the nitriding process. Finally, all the associated physical modifications (grain refining, stress, and texture) contribute to a more efficient nitriding diffusion process, increasing the material hardness. The experimental results obtained with the atomic attrition procedure show that the nitriding time could be shortened.

Acknowledgments

Part of this work was supported by FAPESP, project # 2013/12501-4. FA, CAF, LFZ and MM are CNPq and Capes fellows, respectively. The authors are indebted to the Brazilian Synchrotron Light Laboratory (LNLS) where the grazing X-ray experiments were performed.

References

[1] R. Wei, Surf. Coat. Technol. 83 (1996) 218–227.
[2] T. Czerwiec, H. Michel, E. Bergman, Surf. Coat. Technol. 108 (1998) 182–190.
[3] K.T. Rie, E. Menthe, A. Matthews, K. Legg, J. Chin, MRS Bull. 21 (1996) 46–51.
[4] Z. Wang, E.G. Seebauer, Phys. Rev. Lett. 95 (2005) 015501.
[5] W.P. Tong, N.R. Tao, Z.B. Wang, J. Lu, K. Lu, Science 299 (2003) 686–688.
[6] C. Suryanarayana, Prog. Mater. Sci. 46 (2001) 1–180.
[7] E.A. Ochoa, C.A. Figueroa, T. Czerwiec, F. Alvarez, Appl. Phys. Lett. 88 (2006) 254109.
[8] Q. Jiang, S.H. Zhang, J.C. Li, Sol. Stat. Comm. 130 (2004) 581–584.
[9] G. Abrasonis, W. Möller, X. Ma, Phys. Rev. Lett. 96 (2006) 065901.
[10] L. Zhang, G. Tang, X. Ma, Phys. Lett. A 374 (2010) 2137–2139.
[11] A. Martinavičius, G. Abrasonis, W. Möller, C. Templier, J.P. Rivière, A. Declémy, Y. Chumlyakov, J. Appl. Phys. 105 (2009) 093502.
[12] P. Hammer, N.M. Victoria, F. Alvarez, J. Vac. Sci. Technol. A 16 (1998) 2941–2949.
[13] C.A. Figueroa, D. Wisnivesky, F. Alvarez, J. Appl. Phys. 92 (2002) 764–770.
[14] P. Hammer, N.M. Victoria, F. Alvarez, J. Non-Cryst. Solids 227 (1998) 645–649 and references therein.
[15] W.C. Oliver, G.M. Pharr, J. Mater. Res. 7 (1992) 1564–1583.
[16] S.J. Skrzypek, A. Baczmanski, W. Ratuszek, E. Kusior, J. Appl. Crystallogr. 34 (2001) 427–435 and references therein.
[17] I.C. Noyan, J.B. Cohen, Residual Stress, Springer-Verlag, New York, 1987.
[18] C. Quaeyhaegens, G. Knuyt, L.M. Stals, J. Vac. Sci. Technol. A 14 (1996) 2462–2469.
[19] E.A. Ochoa, C.A. Figueroa, F. Alvarez, J. Vac. Sci. Technol. A 24 (2006) 2113–2116.
[20] F.M. Dheurle, J.M.E. Harper, Thin Solid Films 171 (1989) 81–92; K.-H. Müller, J. Appl. Phys. 62 (1987) 1796–1799.
[21] J. Tarus, K. Nordlund, A. Kurunem, J.P. Keinomen, Phys. Rev. B 58 (15) (1998-I) 9907–9915. S. Pil, H. B. Chew, E. Chason, V. B. Shenoy, K.-S. Kim, Proc. R. Soc. A, http://dx.doi.org/10.1098/rspa.2012.0042.
[22] W.L. Chana, E. Chason, J. Appl. Phys. 101 (2007) 121301.
[23] See:D. Briggs, M.P. Seah (Eds.), second ed.Practical Surface Analysis, vol. 1, J. Wiley, New York, 1996.
[24] J.D. Kamminga, T.H. de Keijser, R. Delhez, J. Appl. Phys. 88 (2000) 6332–6345.
[25] R.W.K. Honeycombe, H.K.D.H. Bhadeshia, Steels: Microstructure and Properties, Edward Arnold Publisher, London, 1995.
[26] P.H. Citrin, D.R. Haman, Phys. Rev. B 10 (1974) 4948–4963.
[27] R.G. Lacerda, M.C. dos Santos, L.R. Tessler, P. Hammer, F. Alvarez, F.C. Marques, Phys. Rev. B 68 (2003) 54104.
[28] K. Siegbahn, C. Nordling, G. Johansson, J. Hedman, P.F. Heden, K. Hamrin, U. Gelius, T. Bergmark, L.O. Werme, R. Manne, Y. Baer, ESCA Applied to Free Molecules, North-Holland, Amsterdam, 1971.
[29] J.P.B. Biersack, G.L. Haggmark, The simulation used the TRIM software, Nucl. Instrum. Methods 174 (1980) 257–269.
[30] R. Menig, V. Schulze, O. Vöhringer, Mat. Sci. Eng. A 335 (2002) 198–206.
[31] C.Q. Sun, W.H. Zhon, S. Li, B.K. Tay, J. Phys. Chem. B 108 (2004) 1080–1084.
[32] F. Seitz, J.S. Koehler, Phys. Status Solidi 2 (1956). Academic Press, New York.
[33] C.A. Davis, Thin Solid Films 226 (1993) 30.
[34] J. Crank, The Mathematics of Diffusion, second ed., Clarendon Press, Oxford, 1975.
[35] K. Morishita, B.D. Wirth, T. Diaz de la Rubia, A. Kimura, in: S. Hanada, Z. Zhong, S.W. Nam, R.N. Wright (Eds.), Proceedings of "The Fourth Pacific Rim International Conference on Advanced Materials and Processing (PRICM4)", vol. I–II, The Japan Institute of Metals, 2001, pp. 1383–1386.
[36] L.F. Zagonel, J. Bettini, R.L.O. Basso, P. Paredez, H. Pinto, C.M. Lepienski, F. Alvarez, Surf. Coat. Technol. 207 (2012) 72–78.
[37] Y.P. Sharkeev, E.V. Kozlov, Surf. Coat. Technol. 158–159 (2002) 219–224.
[38] Y.P. Sharkeev, A.N. Didenko, E.V. Kozlov, Surf. Coat. Technol. 65 (1994) 112–120 and references therein.
[39] R.E. Reed-Hill, Physical Metallurgy Principles, second ed., D. van Nostrand Company, New York, 1973.
[40] T.K. Hirsch, A.Da S. Rocha, F.D. Ramos, T.R. Strohaecker, Metall. Mater. Trans. 35A (2004) 3524–3530.